

## 2. Fundamentals of Radio Interferometry

A. Richard Thompson

*National Radio Astronomy Observatory, Charlottesville, VA 22903, U.S.A.*

### Abstract.

The practical aspects of interferometry are reviewed, starting with a two element interferometer.

### 1. Introduction

In the first lecture, it was shown that images of a distant radio source can be made by measuring the mutual coherence function of the electric fields at pairs of points in a plane normal to the direction to the source. This process can be envisioned by considering a large flat area on the Earth's surface on which antennas are located, and an electronic system including correlators to measure the coherence of the received signals. Now suppose that the Earth does not rotate, and that the source under observation is at the zenith. We can measure the coherence as a function of the spacing between pairs of antennas, independent of the absolute location of the antennas in the antenna plane. Next suppose that the Earth remains fixed relative to the sky, but that the source under investigation is not at the zenith. A wavefront from the source meets the plane in a line that progresses across the plane, and thus does not reach all antennas simultaneously. As a result, we need to include delay elements in the electronic system to ensure that the signals received by different antennas from the same wavefront arrive at the correlators at the same time. The spacings in  $(u, v)$  coordinates are now the components of the baselines projected onto a plane normal to the direction of the source. Finally, consider the effect of the rotation of the Earth. It is necessary for the antenna pointing and the time delays to be continuously adjusted to follow the source across the sky. Further, although at any instant the baselines lie within a plane, this plane is carried through space by the Earth, and its position relative to the source is continuously changing. The non-coplanar distribution of the baselines which thus generally<sup>1</sup> occurs during an extended period of observation can complicate the inversion of the coherence data to obtain an image. On the other hand, the motion of the baseline vectors has the useful effect of reducing the number of antenna locations on the Earth required to measure the coherence over the necessary range of  $(u, v)$  coordinates.

In this lecture the effects described above will be examined in some detail, as part of a discussion of the practical implementation of interferometers and arrays. A number of the relationships derived in the treatment deriving from physical optics will emerge again as expressions for the response of an interferometer. Other discussions of the interferometer response can be found in Swenson & Mathur (1968), Fomalont (1973), Fomalont & Wright (1974), Meeks (1976), Christiansen & Högbom (1985), and Rohlfs (1986); a detailed and extensive review is given by Thompson, Moran & Swenson (1986).

---

<sup>1</sup>Except in the case of an East–West linear array, as will be explained.

## 2. Response of an Interferometer

Synthesis arrays, which produce images by Fourier synthesis from measurements of complex visibility, can be analyzed as ensembles of two-element interferometers. Many of the effects can therefore be understood from a discussion of the properties of a two-element instrument. A simplified block diagram of such an interferometer is shown in Figure 2-1. The two antennas point toward a distant radio source in a direction indicated by unit vector  $\mathbf{s}$ .  $\mathbf{b}$  is the interferometer baseline, and the wavefront from the source reaches one antenna at a time  $\tau_g$  later than the other.  $\tau_g$  is called the *geometrical delay* and is given by

$$\tau_g = \mathbf{b} \cdot \mathbf{s} / c, \quad (2-1)$$

where  $c$  is the speed of light. The signals from the antennas pass through amplifiers which incorporate filters to select the required frequency band of width  $\Delta\nu$  centered on frequency  $\nu$ . The component in which the signals are combined is the *correlator*, which is a voltage multiplier followed by a time averaging (integrating) circuit. If the input waveforms to the correlator are  $V_1(t)$  and  $V_2(t)$ , the output is proportional to

$$\langle V_1(t)V_2(t) \rangle, \quad (2-2)$$

where the angular brackets denote a time average. We can represent the received signals by quasi-monochromatic Fourier components of frequency  $\nu$ , which have the form  $V_1(t) = v_1 \cos 2\pi\nu(t - \tau_g)$  and  $V_2(t) = v_2 \cos 2\pi\nu t$ . The output of the correlator is then

$$r(\tau_g) = v_1 v_2 \cos 2\pi\nu\tau_g. \quad (2-3)$$

$\tau_g$  varies slowly with time as the Earth rotates, and the resulting oscillations of the cosine term in Equation 2-3 represent the motion of the source through the interferometer fringe pattern. We may assume that these oscillations are sufficiently slow that the fringes are not significantly attenuated by the averaging (an expression for the fringe frequency is given in Section 8). In contrast, the component at frequency  $2\nu$  generated in the multiplication is effectively filtered out. Note that the term  $v_1 v_2$ , which represents the fringe amplitude, is proportional to the received power.

We now express the interferometer output in terms of the radio brightness integrated over the sky. Let  $I(\mathbf{s})$  represent the radio brightness in the direction of unit vector  $\mathbf{s}$  at frequency  $\nu$ . The brightness is also sometimes referred to as intensity and is measured in  $\text{W m}^{-2} \text{Hz}^{-1} \text{sr}^{-1}$ . Note that each antenna responds to a component of the input radiation field determined by the antenna polarization. The way in which the antenna polarization is varied to explore the total radiation field is considered in Lectures 3 and 6. The signal power received in bandwidth  $\Delta\nu$  from the source element  $d\Omega$  is  $A(\mathbf{s})I(\mathbf{s})\Delta\nu d\Omega$ , where  $A(\mathbf{s})$  is the effective collecting area in direction  $\mathbf{s}$ , which we assume to be the same for each of the antennas. The resulting output from the correlator is proportional to the received power and to the cosine fringe term. Thus, omitting constant gain factors, we can represent the correlator output for the signal from solid angle  $d\Omega$  by

$$dr = A(\mathbf{s})I(\mathbf{s})\Delta\nu d\Omega \cos 2\pi\nu\tau_g. \quad (2-4)$$

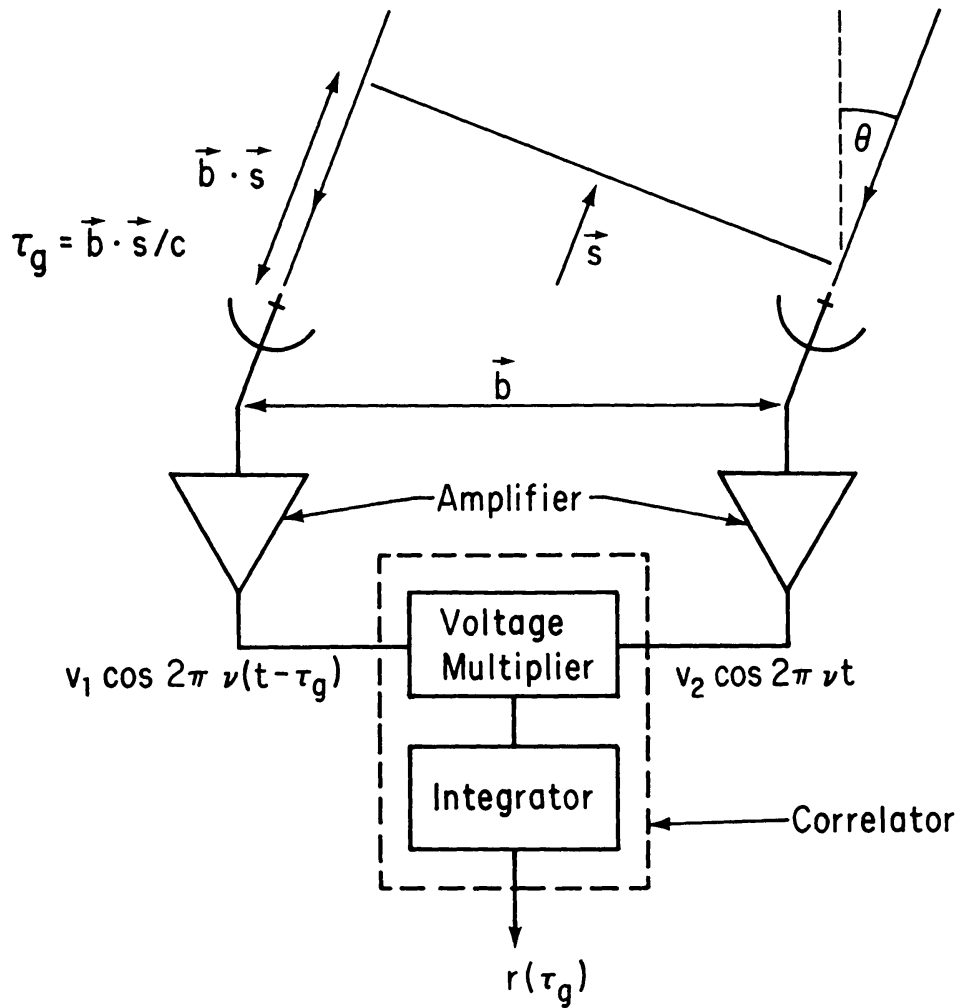
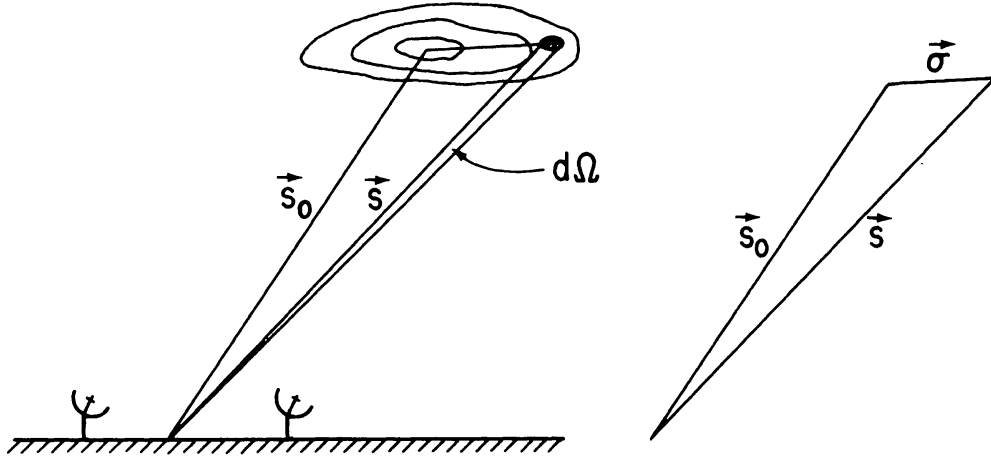


Figure 2-1. Simplified schematic diagram of a two-element interferometer.

In terms of the baseline and source position vectors we can write

$$r = \Delta\nu \int_S A(\mathbf{s}) I(\mathbf{s}) \cos \frac{2\pi\nu \mathbf{b} \cdot \mathbf{s}}{c} d\Omega. \quad (2-5)$$

The integral in Equation 2-5 is taken over the entire surface  $S$  of the celestial sphere, subtending  $4\pi$  steradians, but in practice the integrand usually falls to very low values outside a small angular field as a result of the antenna beamwidth, the finite dimensions of the radio source, and other effects which restrict the field of view (see Sections 10 and 11, and Lecture 13). We assume that the bandwidth  $\Delta\nu$  is sufficiently small that variation of  $A$  and  $I$  with  $\nu$  can be ignored. Two further assumptions have been made in deriving Equation 2-5. First, the source must be in the far field of the interferometer so that the incoming wavefronts can be considered to be plane. With the longest spacings and shortest wavelengths commonly in use, this condition may not be met by some objects within the solar system. Second, the assumption that the responses from different points in the source can be added independently is implicit in the



**Figure 2-2.** Position vectors used in deriving the interferometer response to a source. The source is represented by the contours of radio brightness  $I(\mathbf{s})$  on the sky.

integration over angle in Equation 2-5. This requires that the source be spatially incoherent—i.e., that signal components emanating from different points on the source be uncorrelated.

When taking observations to make an interferometric image of a radio source, it is usual to specify a position on which the synthesized field of view is to be centered. This position is commonly referred to as the *phase tracking center* or *phase reference position*. We can represent this position by the vector  $\mathbf{s}_0$ , as shown in Figure 2-2, and write  $\mathbf{s} = \mathbf{s}_0 + \boldsymbol{\sigma}$ . From Equation 2-5 we then obtain

$$\begin{aligned} r &= \Delta\nu \cos\left(\frac{2\pi\nu \mathbf{b} \cdot \mathbf{s}_0}{c}\right) \int_S A(\boldsymbol{\sigma}) I(\boldsymbol{\sigma}) \cos \frac{2\pi\nu \mathbf{b} \cdot \boldsymbol{\sigma}}{c} d\Omega \\ &- \Delta\nu \sin\left(\frac{2\pi\nu \mathbf{b} \cdot \mathbf{s}_0}{c}\right) \int_S A(\boldsymbol{\sigma}) I(\boldsymbol{\sigma}) \sin \frac{2\pi\nu \mathbf{b} \cdot \boldsymbol{\sigma}}{c} d\Omega. \end{aligned} \quad (2-6)$$

We now introduce the *visibility*, which is a measure of the coherence discussed in Lecture 1. The term visibility was first used in interferometry by Michelson (1890) to express the relative amplitude of the optical fringes that he observed. As used in radio astronomy, visibility is a complex quantity, the magnitude of which has the dimensions of spectral power flux density ( $\text{W m}^{-2} \text{Hz}^{-1}$ ). It can be regarded as an unnormalized measure of the coherence of the electric field, modified to some extent by the characteristics of the interferometer.

The complex visibility of the source is defined as

$$V \equiv |V| e^{i\phi_V} = \int_S \mathcal{A}(\boldsymbol{\sigma}) I(\boldsymbol{\sigma}) e^{-2\pi i \nu \mathbf{b} \cdot \boldsymbol{\sigma} / c} d\Omega \quad (2-7)$$

where  $\mathcal{A}(\boldsymbol{\sigma}) \equiv A(\boldsymbol{\sigma})/A_0$  is the normalized antenna reception pattern,  $A_0$  being the response at the beam center. We are considering the case in which the antennas track the source, and the system therefore responds to the modified

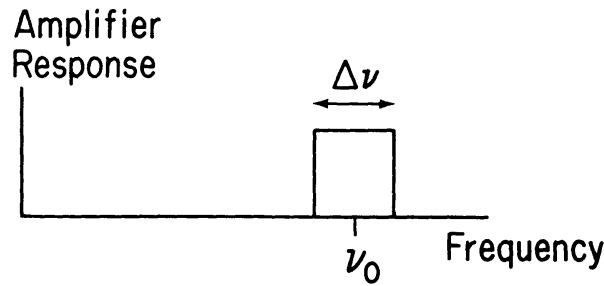


**Figure 2-3.** Idealized rectangular response of the receiving system.

brightness distribution  $\mathcal{A}(\sigma)I(\sigma)$ . By separating the real and imaginary parts of  $V$  in Equation 2-7 we obtain

$$A_0|V|\cos\phi_V = \int_S A(\sigma)I(\sigma) \cos \frac{2\pi\nu \mathbf{b} \cdot \boldsymbol{\sigma}}{c} d\Omega \quad (2-8)$$

and

$$A_0|V|\sin\phi_V = - \int_S A(\sigma)I(\sigma) \sin \frac{2\pi\nu \mathbf{b} \cdot \boldsymbol{\sigma}}{c} d\Omega. \quad (2-9)$$

Substitution of Equations 2-8 and 2-9 into Equation 2-6 gives

$$r = A_0\Delta\nu|V|\cos\left(\frac{2\pi\nu \mathbf{b} \cdot \mathbf{s}_0}{c} - \phi_V\right). \quad (2-10)$$

In the interpretation of interferometer measurements the usual procedure is to measure the amplitude and phase of the fringe pattern as represented by the cosine term in Equation 2-10, and then derive the amplitude and phase of  $V$  by appropriate calibration. The brightness distribution of the source is obtained from the visibility data by inversion of the transformation in Equation 2-7. Thus  $V$  must be measured over a sufficiently wide range of  $\nu\mathbf{b} \cdot \boldsymbol{\sigma}/c$ , which is the component of the baseline normal to the direction of the source and measured in wavelengths. This component can be envisaged as the baseline viewed from the direction of the source.

### 3. Effect of Bandwidth in a Two-Element Interferometer

Since the frequency of the cosine fringe term in Equation 2-10 is proportional to the observing frequency  $\nu$ , observing with a finite bandwidth  $\Delta\nu$  results, in effect, in the combination of fringe patterns with a corresponding range of fringe frequencies. For the response with an infinitesimal bandwidth  $d\nu$  we can write, from Equations 2-1 and 2-10,

$$dr = A_0|V|\cos(2\pi\nu\tau_g - \phi_V) d\nu. \quad (2-11)$$

Then for a rectangular frequency passband, as shown in Figure 2-3, the interferometer response is

$$r = A_0|V| \int_{\nu_0 - \Delta\nu/2}^{\nu_0 + \Delta\nu/2} \cos(2\pi\nu\tau_g - \phi_V) d\nu$$

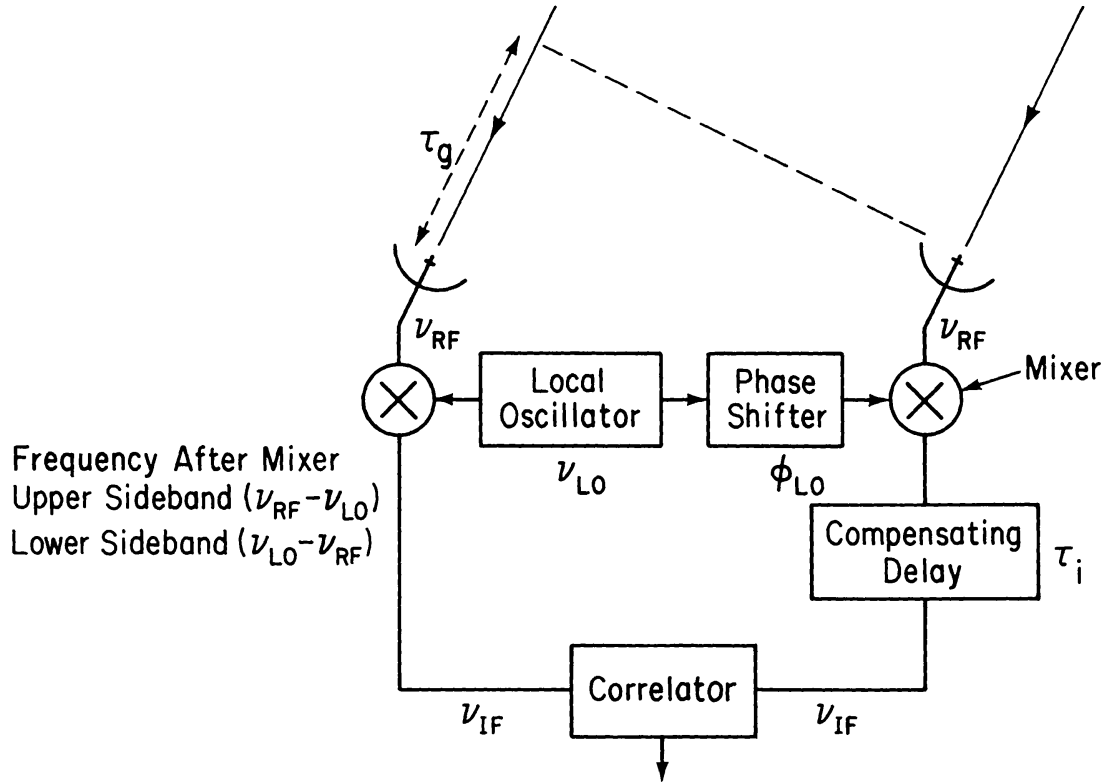


**Figure 2-4.** Simplified schematic diagram of an interferometer system incorporating frequency conversion and an instrumental time delay to compensate for  $\tau_g$ . For simplicity, the amplifiers and filters are omitted.

$$= A_0 |V| \Delta\nu \frac{\sin \pi \Delta\nu \tau_g}{\pi \Delta\nu \tau_g} \cos (2\pi \nu_0 \tau_g - \phi_V), \quad (2-12)$$

where  $\nu_0$  is the center frequency of the observing passband. Thus in the system that we are considering the fringes are modulated by a sinc-function envelope, sometimes referred to as the *bandwidth pattern*. The full fringe amplitude is observed only when the source is in a direction normal to the baseline so that  $\tau_g = 0$ . The range of  $\tau_g$  for which the fringe amplitude is within, say, 1% of the maximum value can be obtained by writing

$$\frac{\sin \pi \Delta\nu \tau_g}{\pi \Delta\nu \tau_g} \approx 1 - \frac{(\pi \Delta\nu \tau_g)^2}{6} > 0.99 \quad (2-13)$$

which yields  $|\Delta\nu \tau_g| < 0.078$ , where the approximation in Equation 2-13 is valid for  $|\pi \Delta\nu \tau_g| \ll 1$ . The angular range of  $\tau_g$  within this limit depends upon the length and orientation of the baseline: for example, with  $\Delta\nu = 50$  MHz and  $|\mathbf{b}| = 1$  km, the response falls by 1% when the angle  $\theta$  in Fig. 2-1 is 2 arcmin. In order to observe a source over a wide range of hour-angle, it is necessary to include within the system a computer-controlled delay to compensate for  $\tau_g$ .

#### 4. Delay Tracking and Frequency Conversion

A block diagram of an interferometer system that includes an instrumental compensating delay is shown in Figure 2-4. Frequency conversion of the incoming signals at radio frequency  $\nu_{\text{RF}}$  with a local oscillator at frequency  $\nu_{\text{LO}}$  is also included. Practical receiving systems incorporate frequency conversion because it is technically more convenient to perform such functions as amplification, filtering, delaying, and cross-correlating of the signals at an intermediate frequency that is lower than  $\nu_{\text{RF}}$  and remains fixed when the observing frequency is changed. The signals at the frequencies  $\nu_{\text{RF}}$  and  $\nu_{\text{LO}}$  are combined in a mixer which contains a non-linear element (usually a diode) in which combinations of the two frequencies are formed. The intermediate frequency  $\nu_{\text{IF}}$  is related to the mixer input frequencies by

$$\nu_{\text{RF}} = \nu_{\text{LO}} \pm \nu_{\text{IF}}. \quad (2-14)$$

Note that  $\nu_{\text{LO}}$  is a single-valued frequency, but  $\nu_{\text{RF}}$  and  $\nu_{\text{IF}}$  refer to bands of width  $\Delta\nu$ . Thus the mixer responds to inputs in two frequency bands, as shown in Figure 2-5: these are referred to as the upper and lower sidebands and correspond to the  $+$  and  $-$  signs in Equation 2-14 respectively. For observations at frequencies up to a few tens of gigahertz the signal from each antenna is usually first applied to a low-noise amplifier to obtain high sensitivity, and then passed through a filter that transmits only one of the two sidebands to the mixer. The response of such a single-sideband system can be obtained by considering the phase changes  $\phi_1$  and  $\phi_2$  imposed upon the signals received by antennas 1 and 2 before reaching the correlator inputs. For the upper sideband case we have

$$\begin{aligned} \phi_1 &= 2\pi\nu_{\text{RF}}\tau_g = 2\pi(\nu_{\text{LO}} + \nu_{\text{IF}})\tau_g, \\ \phi_2 &= 2\pi\nu_{\text{IF}}\tau_i + \phi_{\text{LO}}, \end{aligned} \quad (2-15)$$

where  $\phi_{\text{LO}}$  is the difference in the phase of the local oscillator signal at the two mixers, and  $\tau_i$  is the instrumental delay that compensates for  $\tau_g$ . The upper-sideband response of the interferometer is obtained by replacing the argument of the cosine function in Equation 2-11 by  $\phi_1 - \phi_2 = -\phi_V$ ,  $d\nu$  by  $d\nu_{\text{IF}}$ , and integrating with respect to  $\nu_{\text{IF}}$  from  $\nu_{\text{IF}_0} - \Delta\nu/2$  to  $\nu_{\text{IF}_0} + \Delta\nu/2$ . Thus:

$$r_u = A_0\Delta\nu|V| \frac{\sin \pi \Delta\nu \Delta\tau}{\pi \Delta\nu \Delta\tau} \cos[2\pi(\nu_{\text{LO}}\tau_g + \nu_{\text{IF}_0}\Delta\tau) - \phi_V - \phi_{\text{LO}}]. \quad (2-16)$$

Here  $\Delta\tau = \tau_g - \tau_i$  is the tracking error of the compensating delay  $\tau_i$ . Note that the output fringe oscillations, which result from the time variation of  $\tau_g$ , in this case depend upon the local oscillator frequency  $\nu_{\text{LO}}$  rather than the observing frequency at the antenna as in Equation 2-10. For the case in which the lower sideband is the one that is accepted by the receiving system we have:

$$\begin{aligned} \phi_1 &= -2\pi(\nu_{\text{LO}} - \nu_{\text{IF}})\tau_g, \\ \phi_2 &= 2\pi\nu_{\text{IF}}\tau_i - \phi_{\text{LO}}, \end{aligned} \quad (2-17)$$

whence

$$r_l = A_0\Delta\nu|V| \frac{\sin \pi \Delta\nu \Delta\tau}{\pi \Delta\nu \Delta\tau} \cos[2\pi(\nu_{\text{LO}}\tau_g - \nu_{\text{IF}_0}\Delta\tau) - \phi_V - \phi_{\text{LO}}]. \quad (2-18)$$

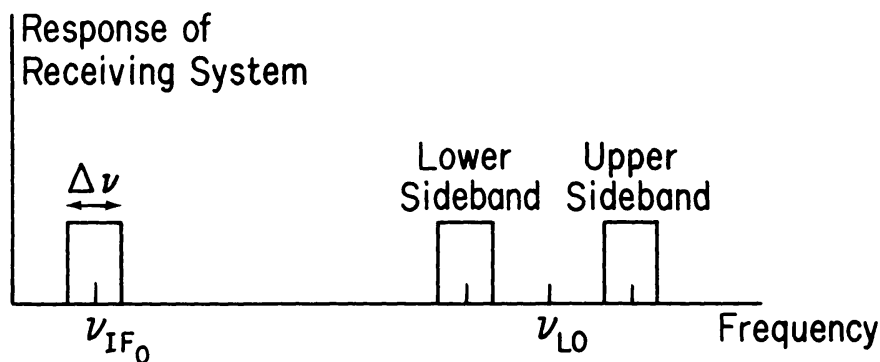


**Figure 2-5.** Relationship of RF (upper and lower sideband), IF, and LO frequencies.

Here the differences in the signs of the various terms compared with those in Equation 2-15 occur because in lower sideband conversion a change in phase of the RF signal causes a phase change of opposite sign in the IF signal. The phase of the local oscillator also enters with a different sign in Equation 2-15 and 2-17.

At frequencies approaching 100 GHz and higher, it is difficult to make low-noise amplifiers to place ahead of the mixers. Often the antenna is connected directly to the mixer input, without any filter to reject one sideband since such a filter can introduce noise unless cryogenically cooled. The result is a double-sideband system, and the response is obtained from the sum of Equation 2-16 and 2-18:

$$\begin{aligned}
 r_d &= r_u + r_l \\
 &= 2\Delta\nu A_0 |V| \frac{\sin(\pi\Delta\nu\Delta\tau)}{\pi\Delta\nu\Delta\tau} \cos(2\pi\nu_{LO}\tau_g - \phi_V - \phi_{LO}) \cos(2\pi\nu_{IF_0}\Delta\tau).
 \end{aligned}
 \tag{2-19}$$

Note that the delay-tracking error  $\Delta\tau$  does not affect the phase of the cosine fringe term as it does in Equation 2-16 and 2-18, but here it appears in a separate cosine term that modulates the amplitude of the fringes. As a result, the double-sideband system requires more critical adjustment of the instrumental delay to maintain the visibility amplitude than does the single-sideband system. Other disadvantages of the double-sideband system include greater vulnerability to interference, and complication of spectral line observations since the spectra of the two sidebands are superimposed. Separation of the sideband responses after correlation of the signals by a technique involving periodic insertion of  $\pi/2$  phase shifts in the local oscillator is used in some instruments: for a discussion see Thompson, Moran & Swenson (1986).

## 5. Fringe Rotation and Complex Correlators

The output from the correlator represented by Equation 2-16, 18 or 19 is fed to a computer which performs some form of optimal analysis to determine the amplitude and phase of the fringe oscillations. The fringe visibility  $V$  can then be obtained by calibration of the instrumental parameters. This calibration usually involves observation of one or more sources with known positions, flux



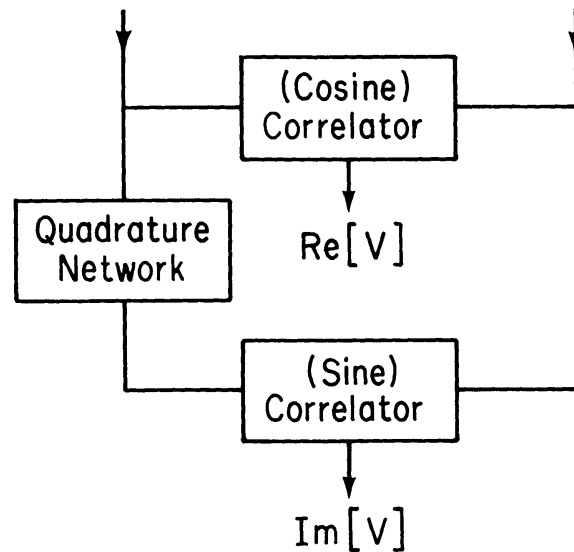


**Figure 2-6.** Complex correlator system. The quadrature network introduces a  $\pi/2$  phase shift: a signal of the form  $\cos 2\pi\nu t$  at its input becomes  $\cos(2\pi\nu t - \pi/2)$  at the output.

densities, and angular dimensions. For an array such as the VLA, the frequencies of the fringe oscillations can exceed 150 Hz for the longest antenna spacings, and in VLBI the fringe frequency can exceed 100 kHz. To preserve the fringe information it is necessary to sample the correlator output at least twice per fringe period. Thus the data rate to the computer can be very much higher than that necessary to follow the changes in the visibility  $V$ , for which values at intervals of order one second are likely to be adequate. However, by inserting progressively varying phase shifts in the local oscillator signals it is possible to slow down the fringe oscillations, and reduce the computation required. Thus in Equation 2-16, 2-18 and 2-19, if we vary  $\phi_{LO}$  so that  $(2\pi\nu_{LO}\tau_g - \phi_{LO})$  remains constant, the correlator output will vary only as a result of changes in  $V$  and slow drifts in the instrumental parameters. This procedure, in which  $\phi_{LO}$  is usually controlled by the same computer that regulates the delay tracking, is variously referred to as *fringe rotation* or *fringe stopping*. Note that the effect of the compensating delay  $\tau_i$  tracking  $\tau_g$  is to cause the envelope of the fringe pattern to follow the source across the sky, and to change the frequency of the fringes by a factor  $\nu_{LO}/\nu_0$  for a single-sideband receiving system. If  $\tau_i$  were inserted at the received signal frequency, the fringe frequency would be reduced to zero without adjustment of the local oscillator phase.

After fringe stopping, the output of the correlator in Figure 2-4 is a slowly varying voltage (a constant voltage for the case of a point source at the phase tracking center). To measure the complex fringe amplitude in this case, a scheme using two correlators, as shown in Figure 2-5 can be used. For each antenna pair a second correlator with a  $\pi/2$  phase shift in one input is added. The response of the second correlator can be obtained by replacing  $\phi_1$  in Equations 2-15 and 2-17 by  $\phi_1 - \pi/2$ . Then in Equations 2-16, 2-18 and 2-19 the cosine term containing  $\tau_g$  becomes a sine, with no change in the argument. The two

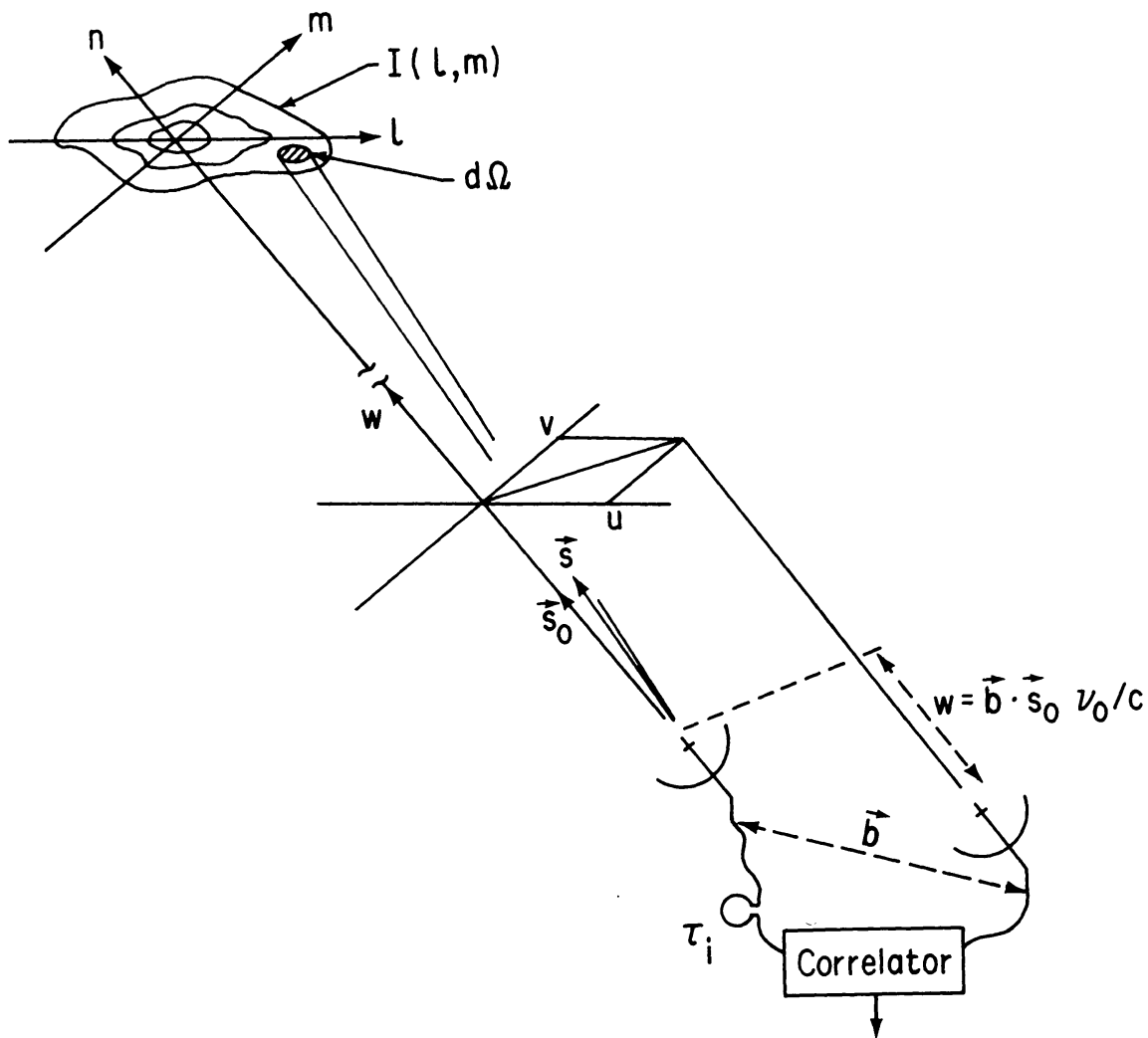


**Figure 2-7.** The  $(u, v, w)$  and  $(l, m, n)$  right-handed coordinate systems used to express the interferometer baselines and the source brightness distribution, respectively.

outputs in Figure 2-6 can thus be regarded as measuring the real and imaginary parts of the complex fringe amplitude, or complex visibility. Such a scheme is usually referred to as a *complex correlator*. In addition to allowing the visibility to be measured with zero fringe frequency, the complex correlator provides an improvement of  $\sqrt{2}$  in signal-to-noise ratio over a single correlator, since the noise fluctuations at the two outputs are uncorrelated. See Lecture 9 for an analysis of signal-to-noise ratios.

## 6. Phase Switching

Phase switching is a technique that is included in many interferometer systems to eliminate errors in the form of constant or slowly varying offsets in the correlator outputs. Such errors can result from misadjustment of the correlator circuitry, cross coupling between the signals at the correlator inputs, and various other

effects. They can be very effectively reduced by periodically reversing the phase of one of the signals at an early point in the receiving system, and synchronously reversing the sign of the multiplier output in the correlator, before the data are averaged. For the wanted component of the signal, the two reversals cancel one another, but unwanted components in the multiplier output which do not reverse sign with reversal of the phase of a received signal are averaged towards zero. In practice, the frequency of the switching is of the order of 10 or 100 Hz. This technique, known as phase switching, was first introduced by Ryle (1952) as a means of implementing the multiplicative action of a correlator using a power-linear diode detector. For a description of a more recent application of phase switching see Granlund, Thompson & Clark (1978).

## 7. Coordinate Systems for Imaging

The practical application of Equation 2-7 requires the introduction of a coordinate system, and the one that is usually chosen was introduced in Lecture 1 and is shown in Figure 2-7. The baseline vector has components  $(u, v, w)$  where  $w$  points in the direction of interest, i.e., towards a position  $\mathbf{s}_0$  that becomes the center of the synthesized image. Note that  $u$ ,  $v$ , and  $w$  are measured in wavelengths at the center frequency of the RF signal band, and in directions towards the East, the North, and the phase tracking center, respectively. Positions on the sky are defined in  $l$  and  $m$ , which are direction cosines measured with respect to the  $u$  and  $v$  axes. A synthesized image in the  $(l, m)$  plane represents a projection of the celestial sphere onto a tangent plane at the  $(l, m)$  origin. Distances in  $l$  and  $m$  are proportional to the sines of the angles measured from the origin, which is a convenient practical system. In these coordinates the parameters used in the derivation of the interferometer response in terms of visibility (Eqs. 6 and 7) become

$$\begin{aligned} \frac{\nu \mathbf{b} \cdot \mathbf{s}}{c} &= ul + vm + wn, \\ \frac{\nu \mathbf{b} \cdot \mathbf{s}_0}{c} &= w, \\ \text{and} \quad d\Omega &= \frac{dl \, dm}{n} = \frac{dl \, dm}{\sqrt{1 - l^2 - m^2}}. \end{aligned} \quad (2-20)$$

Thus in the coordinates of Figure 2-7, Equation 2-7 becomes

$$V(u, v, w) = \int_{-\infty}^{\infty} \int_{-\infty}^{\infty} \mathcal{A}(l, m) I(l, m) e^{-2\pi i [ul + vm + w(\sqrt{1 - l^2 - m^2} - 1)]} \frac{dl \, dm}{\sqrt{1 - l^2 - m^2}}, \quad (2-21)$$

where the integrand is taken to be zero for  $l^2 + m^2 \geq 1$ . Note that we express the complex visibility as a function of  $(u, v, w)$ , since these are the coordinates that represent the spacings of the antennas with respect to the phase tracking center of the source,  $\mathbf{s}_0$ . The visibility is also a function of the modified brightness distribution  $\mathcal{A}I$ .

To simplify the inversion of Equation 2-21, by means of which  $I(l, m)$  is obtained from the visibility, it is desirable to reduce this equation to the form

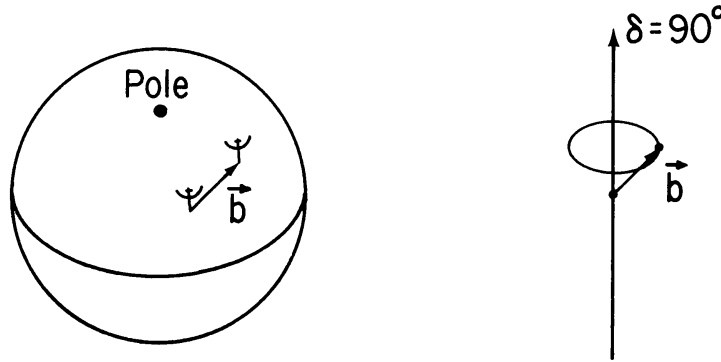


**Figure 2-8.** As the Earth rotates, the baseline vector  $\mathbf{b}$ , which represents the spacing of the two antennas, traces out a circular locus in a plane normal to the direction of declination ( $\delta$ ) equal to  $90^\circ$ . If the antennas are in an East-West line on the Earth, then the vector  $\mathbf{b}$  is normal to the rotation axis.

of a two-dimensional Fourier transform. This can be done under two sets of conditions. The first is when the baselines are coplanar, which can be understood by considering the way in which the Earth's rotation carries the antennas through space. It should be evident from Figure 2-8 that the rotation causes the tip of the baseline vector to trace out a circle concentric with the Earth's rotation axis. The rising and setting of a point on the sky usually limit the range over which  $V$  can be measured to an arc of the circle. In general, for a two-dimensional array of antennas on the surface of the Earth, the circular loci resulting from the different baselines have different diameters and lie in different planes. However, for the particular case of an array of antennas in an East-West line on the Earth's surface, the components of the baseline vector parallel to the Earth's axis are zero, and the baseline-vectors are coplanar. Then, if we choose the  $w$ -axis to lie in the direction of the celestial pole, so that  $w = 0$ , Equation 2-21 becomes

$$V(u, v) = \int_{-\infty}^{\infty} \int_{-\infty}^{\infty} \mathcal{A}(l, m) I(l, m) e^{-2\pi i(ul+vm)} \frac{dl dm}{\sqrt{1-l^2-m^2}}. \quad (2-22)$$

This equation is a two-dimensional Fourier transform, the inverse of which is

$$\frac{\mathcal{A}(l, m) I(l, m)}{\sqrt{1-l^2-m^2}} = \int_{-\infty}^{\infty} \int_{-\infty}^{\infty} V(u, v) e^{2\pi i(ul+vm)} du dv. \quad (2-23)$$

Equation 2-23 can be applied to all parts of the hemisphere shown in Figure 2-9. Usually we want to image a small area of the sky defined by the antenna beams. If this is centered on right ascension  $\alpha_0$  and declination  $\delta_0$ , we can choose the direction of the  $u$ -axis as in Figure 2-9 so that  $l$  is small within the region of interest and is approximately equal to angular distance on the sky. However,  $m$  remains the sine of the angular distance measured from the pole, i.e.,  $m = \cos \delta$ , and the scale of the image is compressed in the  $m$ -direction by a factor  $\sin \delta$ . Thus one would prefer to center the image on  $(\alpha_0, \delta_0)$ . This can be done by rotating the axes about the  $u$ -direction until  $w$  points towards  $(\alpha_0, \delta_0)$

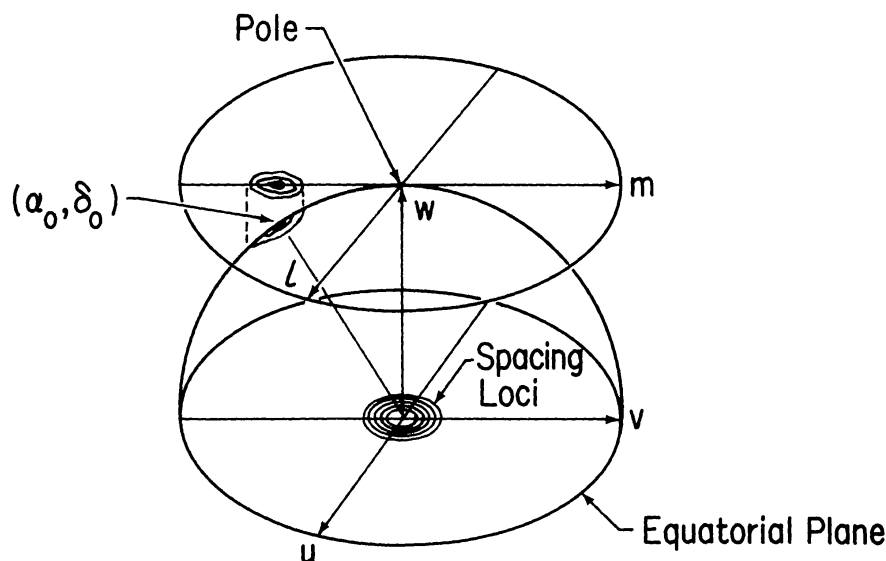


**Figure 2–9.** Celestial hemisphere showing the projection of a source at  $(\alpha_0, \delta_0)$  onto the tangent plane at the pole. The spacing-vector loci are for an array with East–West baselines, and lie in a plane parallel to the Earth’s equator. The direction of the  $w$ -axis is here chosen to be that of the pole ( $\delta = 90^\circ$ ).

and substituting in Equation 2-21  $w = -v \cos \delta_0$ , which follows from the location of the baselines in the equatorial plane. Then  $m$  can be redefined to provide a two-dimensional Fourier transform relationship. This procedure is required only for large field images, and in most cases the small field approximation, which will be described next, suffices.

It is clear from Figure 2-9 that for an East-West array the projected spacings of the antenna pairs become seriously foreshortened in the  $v$ -direction for the observations at low declinations. In that part of the sky it is necessary to use baselines with a significant component parallel to the Earth's axis, i.e., non-East-West baselines. Thus for a two-dimensional array of antennas the baseline vectors do not remain coplanar in  $(u, v, w)$  space. A system of three coordinates is required to accommodate the spacing vectors, and we must consider the second set of conditions under which Equation 2-21 reduces to a two-dimensional Fourier transform. These depend upon  $|l|$  and  $|m|$  being small enough that we can write

$$\left(\sqrt{1-l^2-m^2}-1\right)w \approx -\frac{1}{2}(l^2+m^2)w \approx 0. \quad (2-24)$$

Then Equation 2-21 becomes

$$V(u, v) = \int_{-\infty}^{\infty} \int_{-\infty}^{\infty} \mathcal{A}(l, m) I(l, m) e^{-2\pi i(ul+vm)} dl dm. \quad (2-25)$$

For  $|l|$  and  $|m|$  small, i.e., small field imaging, the dependence of the visibility upon  $w$  is very small and can be omitted. From Equation 2-25 we can write

$$\mathcal{A}(l, m)I(l, m) = \int_{-\infty}^{\infty} \int_{-\infty}^{\infty} V(u, v) e^{2\pi i(ul+vm)} du dv. \quad (2-26)$$

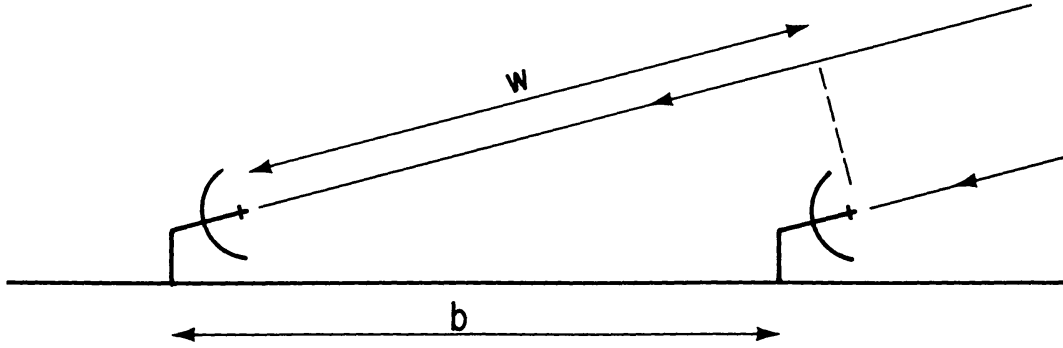


**Figure 2-10.** Comparison of the  $w$ -component and the antenna spacing when the direction of the source is close to that of the baseline. This condition can occur when the source is rising or setting.

For arrays in which the baselines do not remain coplanar as the Earth rotates, the approximation in Equation 2-24 results in a phase error of  $\pi(l^2 + m^2)w$  for radiation from the point  $(l, m)$ . Note that the condition for the approximation in Equation 2-24 to be valid is  $|\pi(l^2 + m^2)w| \ll 1$ , not just  $l^2 + m^2 \ll 1$ . Unless special procedures are used, this condition places a limit on the size of the source that can be imaged without distortion. The limit can be roughly estimated as follows: For any pair of antennas the maximum value of  $w$  occurs when the source under observation is at a low angle of elevation and an azimuth close to that of the baseline, as shown in Figure 2-10. Under such circumstances  $w$  is approximately equal to  $b/\lambda$ , the baseline length measured in wavelengths. Thus for an array of antennas for which the half-power width of the synthesized beam is  $\theta_{\text{HPBW}}$ , we can write

$$\frac{1}{\theta_{\text{HPBW}}} \approx \frac{b_{\text{max}}}{\lambda} \approx w_{\text{max}}, \quad (2-27)$$

where  $b_{\text{max}}$  is the longest baseline. If  $\theta_F$  is the width of the synthesized field, the maximum phase error is about

$$\frac{\pi\theta_F^2}{4\theta_{\text{HPBW}}}. \quad (2-28)$$

Since this is the *maximum* phase error, we can possibly allow it to be as high as 0.1 radian without introducing serious errors in the image, from which we obtain

$$\theta_F < \frac{1}{3} \sqrt{\theta_{\text{HPBW}}}, \quad (2-29)$$

where the two angles are measured in radians. Then, for example, if  $\theta_{\text{HPBW}} = 2''$ ,  $\theta_F < 5'$ . For fields of greater width than allowed by Equation 2-29 there are ways of avoiding or ameliorating the distortion introduced by the phase errors, at the expense of more complicated algorithms and increased computing—see Lecture 19.

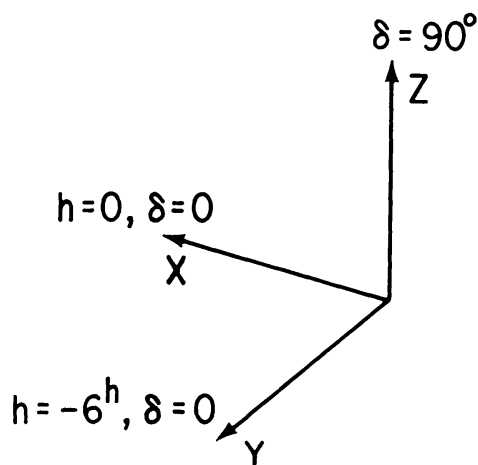


**Figure 2-11.** Coordinate system for specification of baseline parameters.  $X$  is the direction of the meridian at the celestial equator,  $Y$  is toward the East, and  $Z$  toward the North celestial pole.

## 8. Antenna Spacings and $(u, v, w)$ Components

With multiple-element antenna arrays, it is convenient to specify the antenna positions relative to some reference point measured in a Cartesian coordinate system. For example, a system with axes pointing towards hour-angle  $h$  and declination  $\delta$  equal to  $(h = 0, \delta = 0)$  for  $X$ ,  $(h = -6^h, \delta = 0)$  for  $Y$ , and  $(\delta = 90^\circ)$  for  $Z$  may be used as in Figure 2-11. Then if  $L_X$ ,  $L_Y$ , and  $L_Z$  are the corresponding coordinate differences for two antennas, the baseline components  $(u, v, w)$  are given by

$$\begin{pmatrix} u \\ v \\ w \end{pmatrix} = \frac{1}{\lambda} \begin{pmatrix} \sin H_0 & \cos H_0 & 0 \\ -\sin \delta_0 \cos H_0 & \sin \delta_0 \sin H_0 & \cos \delta_0 \\ \cos \delta_0 \cos H_0 & -\cos \delta_0 \sin H_0 & \sin \delta_0 \end{pmatrix} \begin{pmatrix} L_X \\ L_Y \\ L_Z \end{pmatrix}, \quad (2-30)$$

where  $H_0$  and  $\delta_0$  are the hour-angle and declination of the phase reference position, and  $\lambda$  is the wavelength corresponding to the center frequency of the receiving system. The elements in the transformation matrix in Equation 2-30 are the direction cosines of the  $(u, v, w)$  axes relative to  $(X, Y, Z)$  axes: for further details see, e.g., Thompson, Moran & Swenson (1986). By eliminating  $H_0$  from the expressions for  $u$  and  $v$  we obtain the equation of an ellipse in the  $(u, v)$  plane:

$$u^2 + \left( \frac{v - (L_Z/\lambda) \cos \delta_0}{\sin \delta_0} \right)^2 = \frac{L_X^2 + L_Y^2}{\lambda^2}. \quad (2-31)$$

Thus as the interferometer observes a point on the celestial sphere, the rotation of the Earth causes the  $u$  and  $v$  components of the baseline to trace out an elliptical locus. This ellipse is simply the projection onto the  $(u, v)$  plane of the circular locus traced out by the tip of the baseline vector, as shown earlier in Figure 2-8. Since  $I(l, m)$  is real,  $V(-u, -v) = V^*(u, v)$ , and at any instant the correlator output provides a measure of the visibility at two points in the  $(u, v)$

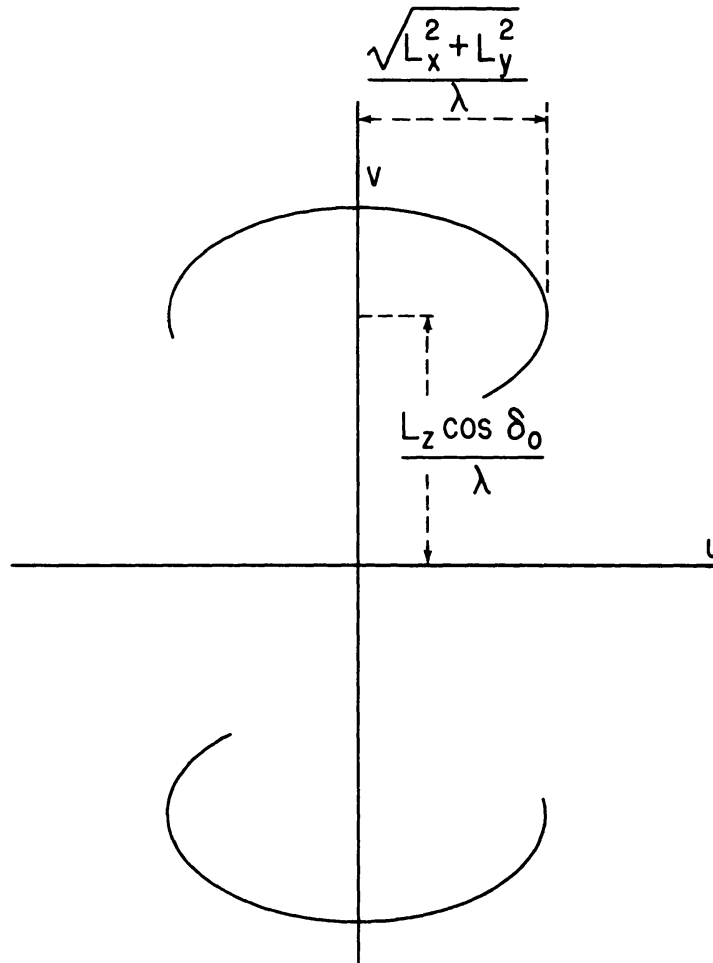


**Figure 2-12.** Elliptical loci representing the projection of the baseline vector onto the  $(u, v)$  plane as a source is tracked across the sky. The lower curve corresponds to a reversal of the direction of the baseline vector, and represents the points for which the visibility is the complex conjugate of that measured on the upper curve. The axial ratio of the ellipses is equal to  $\sin \delta_0$ . For an East-West baseline  $L_Z = 0$ , and a single ellipse is centered on the  $(u, v)$  origin.

plane, as in Figure 2-12. For an array of antennas the ensemble of elliptical loci is known as the *transfer function* or *sampling function*,  $S(u, v)$ , which is a function of the declination of the observation as well as of the antenna spacings. The transfer function indicates the values of  $u$  and  $v$  at which the visibility function is sampled. Since the visibility function for a point source at the  $(l, m)$  origin is a constant in  $u$  and  $v$ , the Fourier transform of the transfer function indicates the response to a point source, i.e., the synthesized beam. In designing arrays the principal aim is to obtain transfer functions that cover the  $(u, v)$  plane as widely and as uniformly as possible. The term transfer function was introduced from an analogy with electrical filter theory. An interferometer responds to structure on the sky with spatial frequency  $u$  cycles per radian in the  $l$ -direction and  $v$  cycles per radian in the  $m$ -direction. The transfer function of an array therefore indicates its response as a spatial frequency filter.



## 9. Astronomical Data from Interferometer Observations

In synthesis imaging an interferometer or array is used to provide values of the complex visibility as a function of  $u$  and  $v$ , from which a brightness distribution can be derived. For this purpose the visibility measurements should be fairly uniformly distributed over the  $(u, v)$  plane, from the origin to some outer boundary that determines the angular resolution. The design of synthesis arrays, which we discuss below, is based largely upon these considerations. If, however, we wish to measure the positions of a series of unresolved sources, the principal consideration is the ability to interpolate the measured visibility phase between one baseline and another, and uniformity of coverage is less important. This consideration also applies to measurements used to monitor universal time, polar motion and geodynamic variation in antenna positions.

In addition to the measurement of complex visibility, two other characteristics of the interferometer output can be used to determine astronomical data. These are principally of importance in VLBI, in which it is not always possible to calibrate the interferometer fringe phase. The first is the bandwidth pattern in Equation 2-12, which can be used to measure  $\tau_g$ . This is accomplished by finding the value of the instrumental delay  $\tau_i$  that maximizes the fringe amplitude. A wide receiver bandwidth, or a series of narrow bands at different frequencies, is used to minimize the width of the fringe envelope as a function of  $\tau_i$  and thereby increase the accuracy. For a source at position  $(H_0, \delta_0)$ ,  $\tau_g$  is equal to  $w/\nu_0$  where  $w$  is given by Equation 2-30. The second characteristic that can be measured is the fringe frequency. Since the relative phase of the signal at the two antennas changes by  $2\pi$  when  $w$  changes by one (wavelength), the fringe frequency is equal to  $dw/dt$ , which can be obtained from Equation 2-30 by differentiation. A useful expression for the fringe frequency  $\nu_F$  is

$$\nu_F = \frac{dw}{dt} = -\omega_e u \cos \delta, \quad (2-32)$$

where  $\omega_e = dH_0/dt$  is the angular rotation velocity of the Earth. Equation 2-32 applies when the instrumental delay  $\tau_i$  is held constant. When  $\tau_i$  tracks  $\tau_g$  a factor  $\nu_0/\nu_{LO}$ ,  $\nu_0$  being the center of the receiving band, should be included for single-sideband receiving systems. In either case,  $\nu_F$  goes through zero on the  $v$ -axis of the  $(u, v)$  plane. Note that a single observation of  $w$  and  $dw/dt$  is sufficient to determine the position of a source if the interferometer baseline is known.

## 10. Design of Synthesis Arrays

In an array of  $n_a$  antennas, a total of  $\frac{1}{2}n_a(n_a - 1)$  pair combinations can be formed. The signal from each antenna is then divided in  $n_a - 1$  ways and fed to a system of correlators. The rate at which visibility measurements can be made, relative to that for a single interferometer, is approximately proportional to  $n_a^2$ . Note that since the signals are amplified before splitting there is no loss in sensitivity, as may occur in instruments for infrared or shorter wavelengths. The primary concern in designing the configuration of antennas is to obtain coverage of the  $(u, v)$  plane (i.e., sampling of the visibility function) as uniformly and efficiently as possible over a range determined by the required angular resolution.

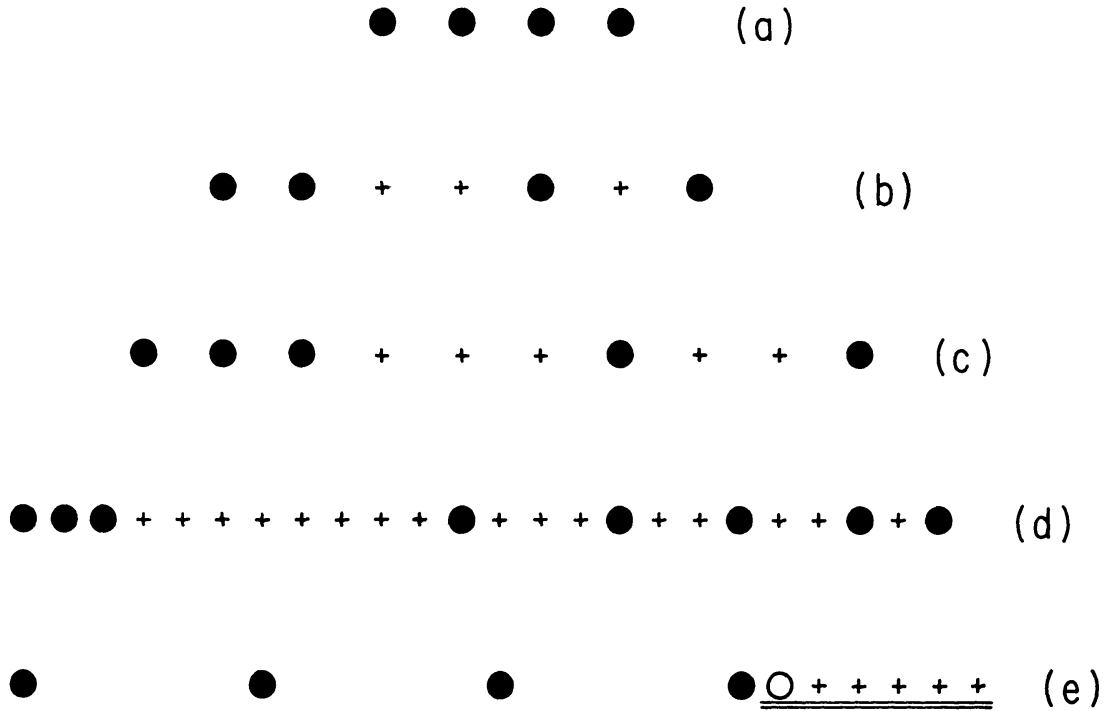


**Figure 2-13.** Examples of several types of linear arrays of antennas. (a) Uniform-spacing array, (b) non-redundant array (Arsac 1955), (c) minimum-redundancy array (Bracewell 1966), (d) minimum-redundancy array (Moffet 1968), and (e) array with movable element represented by the open circle.

A commonly used configuration of antennas for synthesis imaging is an East-West linear array. If the various pair combinations of the antennas encompass a series of spacings which increase by a constant increment, the transfer function consists of a series of ellipses centered on the  $(u, v)$  origin with a constant increment in the major axes. The axial ratios of the ellipses are equal to  $\sin \delta_0$ , as in Figure 2-12, which largely determines the axial ratio of the synthesized beam. Thus, for angular distances greater than about  $30^\circ$  from the celestial equator, East-West linear arrays are satisfactory for two-dimensional imaging. Some basic considerations of linear configurations of antennas are illustrated in Figure 2-13. In a simple, uniformly-spaced array as in (a) the longest spacing is  $n_a - 1$  times the unit spacing. The shorter spacings occur more than once and are highly redundant. Figure 2-13(b) shows a non-redundant arrangement of four antennas designed by Arsac (1955). For more than four antennas there is always some redundancy, as in the example by Bracewell (1966; see also Bracewell *et al.* 1973) in Figure 2-13(c). Other examples of minimum-redundancy arrays are described by Moffet (1968), and an example with eight antennas for which the longest spacing is 23 times the unit spacing is shown in Figure 2-13(d). Only a few such arrays have been constructed for radio astronomy, and configurations with a number of movable antennas, which offer greater flexibility, are generally preferred (see Lecture 27).

Figure 2-13(d) shows an arrangement of four fixed antennas and one movable one. By repeating an observation for each position of the movable antenna, as indicated by the crosses, it is possible to include all baselines up to the overall

length of the array, with intervals equal to the increments in the position of the movable antenna. Although several days are required to complete an observation, a large number of baselines can be covered using a relatively small number of antennas, and highly detailed images obtained. A number of notable instruments have been designed using this principle: these include the One-Mile and Five-Kilometer arrays at Cambridge (Ryle 1962, 1972), the Westerbork Synthesis Radio Telescope (Högbom & Brouw 1974), and the Australia Telescope (Frater 1984). For observations at low declinations, two-dimensional configurations of antennas are generally required to obtain adequate resolution in both right ascension and declination. The design of two-dimensional arrays is more of an empirical matter than that of one-dimensional arrays, since there are no known solutions similar to those based on variability of location of small numbers of antennas or on minimum-redundancy. The main concern is to obtain adequate coverage of the  $(u, v)$  plane, whilst using a fairly simple geometrical configuration for reasons of economy. These considerations are illustrated by the design of the VLA (Thompson *et al.* 1980; Napier, Thompson & Ekers 1983). The antenna configuration and examples of the transfer function for the VLA are shown in Figure 2–14. In the configuration in Figure 2–14a the distance from the center of the array of the  $n^{\text{th}}$  antenna on each arm, counting outwards from the center, is proportional to  $n^{1.716}$ . With this power-law design, no two spacings on any arm are equal. The array is rotated through  $5^\circ$  from the position of North–South symmetry to avoid exact East–West baselines, which would otherwise occur between antennas on the two Southern arms. At declination  $0^\circ$  the  $(u, v)$  components for all East–West baselines become coincident with the  $u$ -axis. Thus the power-law spacing and the rotation are features of the VLA design that reduce redundancy in the coverage of the  $(u, v)$  plane.

The same considerations of uniformity of sampling in the  $(u, v)$  plane also apply to arrays for imaging by VLBI. The main practical difference is that since the antennas are not directly interconnected, except by telephone lines for monitor and control purposes, there is no advantage to any particular geometric pattern. Thus, after the  $(u, v)$  coverage, the main concern is the choice of sites for freedom from interference, low water vapor in the atmosphere, convenience for service, etc. The locations for antennas in the Very Long Baseline Array (VLBA) (Napier *et al.* 1994), and examples of transfer functions, are shown in Figure 2–15. An example of the effect of the addition of the low Earth orbit satellite HALCA to the VLBA is shown in Figure 2–16. The orbital motion significantly increases the resolution along one axis, but at the cost of large holes in the  $(u, v)$  plane. For even longer spacings, it would be possible to use two or more antennas in higher orbits, with periods differing by about 10%, to give a wide distribution of spacings (Preston *et al.* 1983). The subject of orbiting VLBI is more fully discussed in Lecture 26.

## 11. The Effect of Bandwidth in Radio Images

We have seen in Section 2 that the effect of a finite receiving bandwidth  $\Delta\nu$  is to modulate the fringes with an envelope function of width inversely proportional to  $\Delta\nu$ , and that as a result we must insert an instrumental delay  $\tau_i$  to compensate for the geometrical delay  $\tau_g$ . This compensation is exact only for radiation from

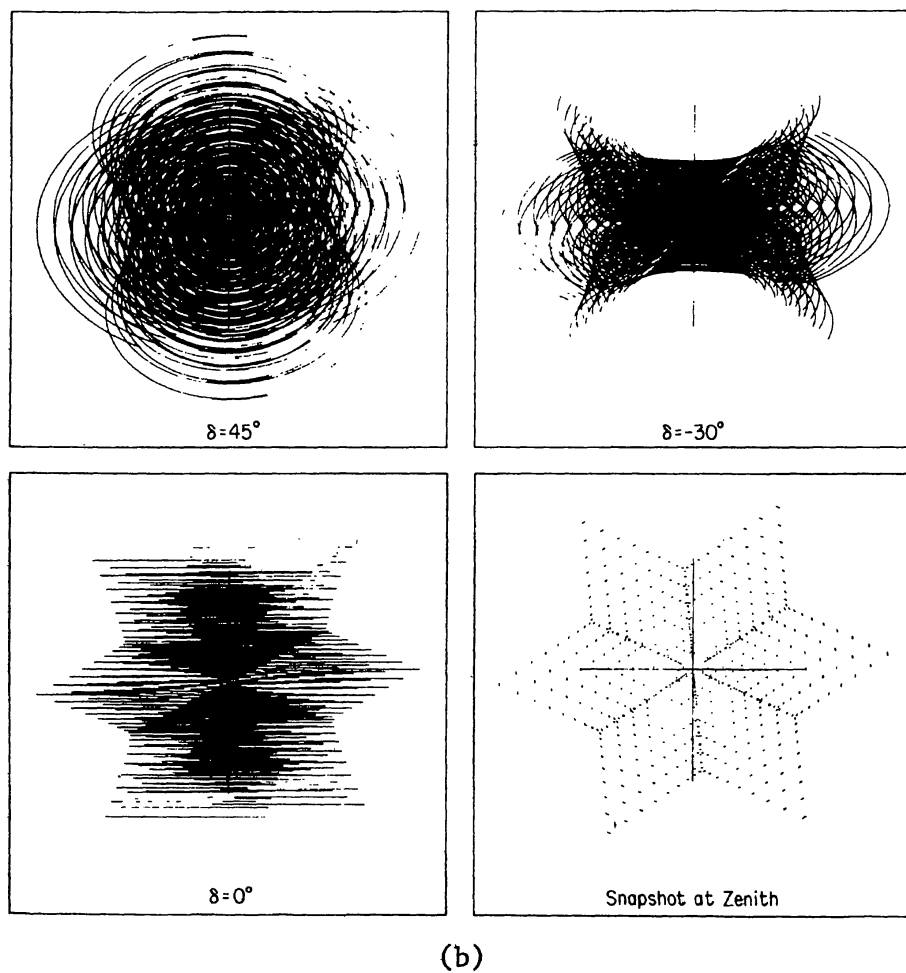
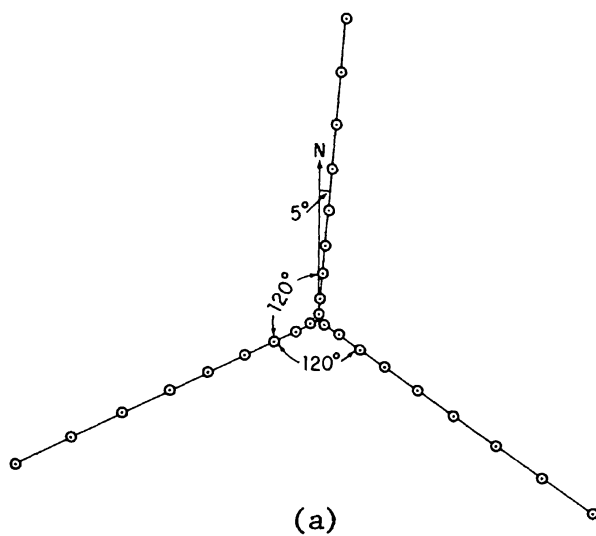
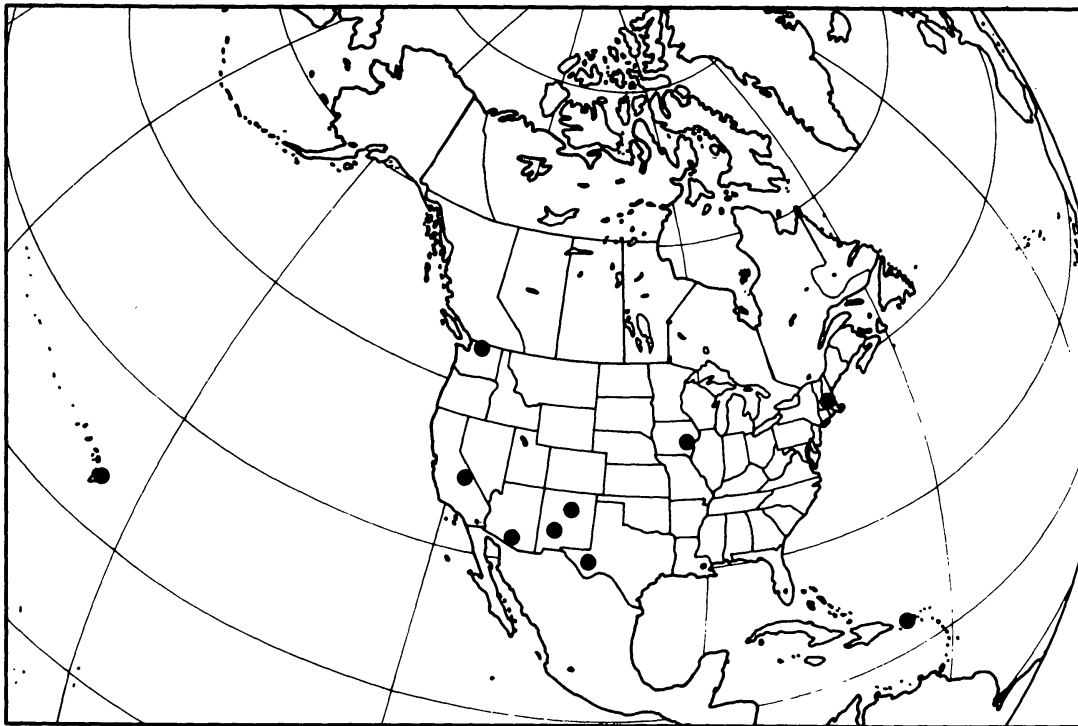
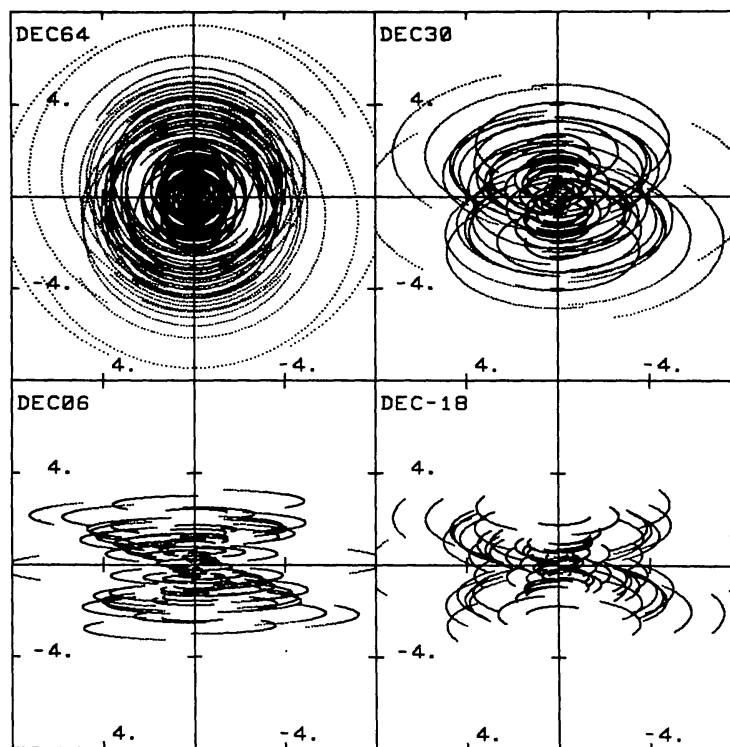


**Figure 2-14.** (a) The configuration of the 27 antennas of the VLA. (b) The transfer functions for four declinations with observing durations of  $\pm 4^{\text{h}}$  for  $\delta = 0^\circ$  and  $45^\circ$ ,  $\pm 3^{\text{h}}$  for  $\delta = -30^\circ$ , and  $\pm 5^{\text{m}}$  for the snapshot. [From Napier, Thompson & Ekers (© 1983 IEEE).]



(a)



(b)

**Figure 2-15.** (a) Locations of the ten antennas of the VLBA, as shown by the closed circles. (b) The corresponding transfer functions for four declinations. [From Walker 1984.]

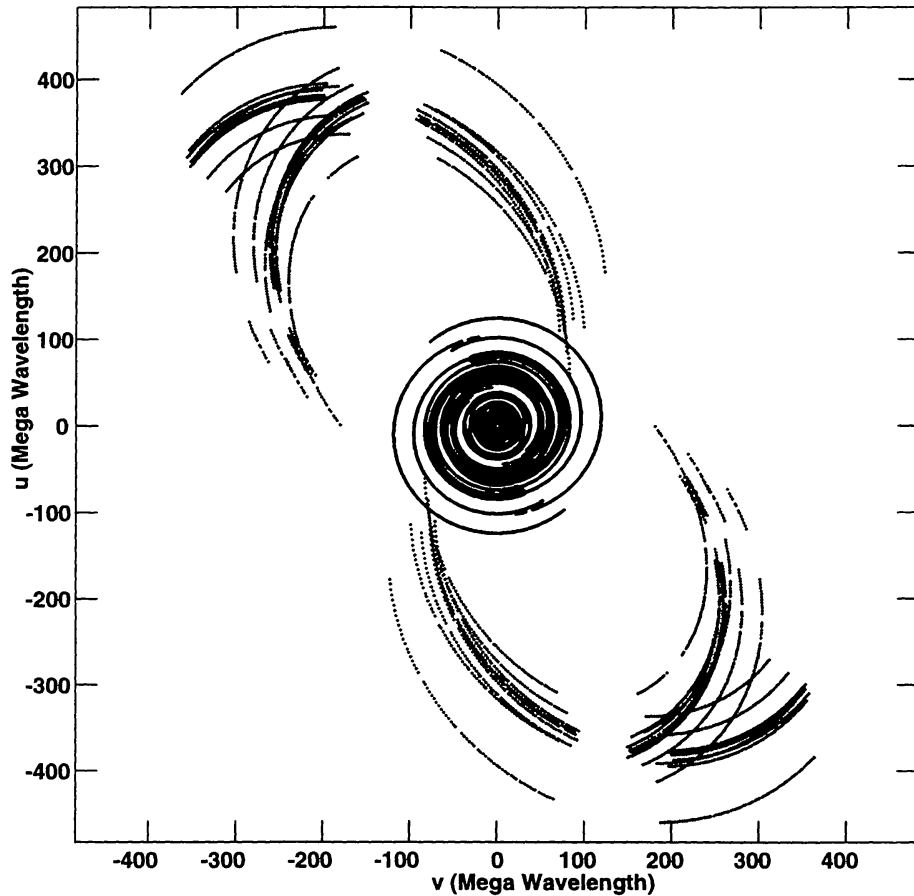


**Figure 2-16.** The  $(u, v)$  coverage provided with the low Earth orbit VLBI satellite HALCA and the ten antennas comprising the VLBA. Three satellite passes are included. The observations were of the northern object 0212+735 at a wavelength of 6cm.

the center of the synthesized field, which is usually chosen as the delay tracking center. Variation of  $\tau_g$  over the field causes a radial blurring of the image (see, e.g., Thompson & D'Addario 1982), as will now be described.

In observing continuum radiation one is interested in the mean brightness over the bandwidth  $\Delta\nu$ , and the visibility data are processed as though they were all observed at the center frequency  $\nu_0$  indicated in Figure 2-17a. In particular, the spatial frequency coordinates in the  $(u, v)$  plane are calculated for the band center. Let these be  $(u_0, v_0)$  for frequency  $\nu_0$  and  $(u, v)$  for another frequency  $\nu$  within the receiving band. Since  $u$  and  $v$  represent projected antenna spacings measured in wavelengths, we can write

$$(u_0, v_0) = \left( \frac{\nu_0}{\nu} u, \frac{\nu_0}{\nu} v \right). \quad (2-33)$$

Now consider the visibility that corresponds to a very small band of frequencies centered on  $\nu$  as in Figure 2-17(a). This band contributes a component of

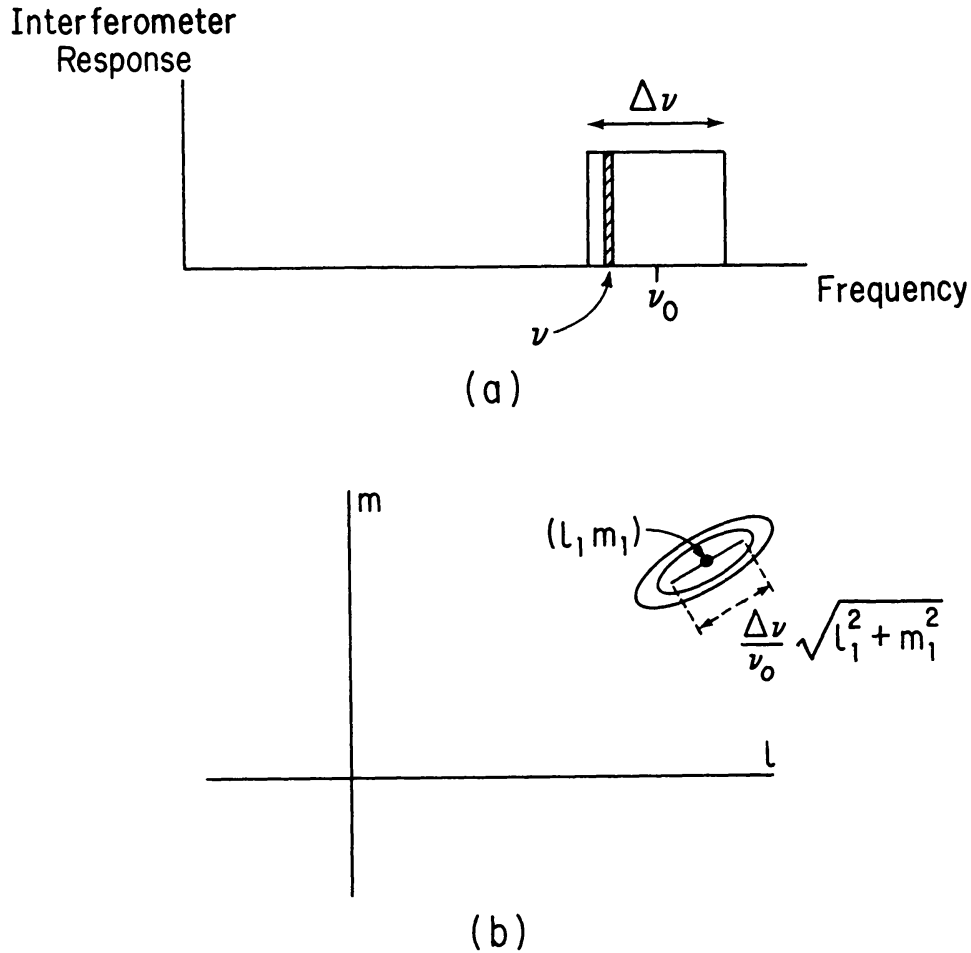


**Figure 2-17.** (a) Idealized rectangular response showing center frequency  $\nu_0$  and a narrow band at frequency  $\nu$ . (b) The radial smearing of a point source at  $(l_1, m_1)$  in the synthesized image.

brightness  $I$  to the synthesized image which is related to the corresponding visibility by

$$V(u, v) \rightleftharpoons I(l, m), \quad (2-34)$$

where the symbol  $\rightleftharpoons$  indicates that the two functions constitute a Fourier transform pair, and we have here omitted the functions  $\mathcal{A}(l, m)$  and  $1/\sqrt{1-l^2-m^2}$  which are usually close to unity. Note that the processes of correlation and Fourier transformation are linear, and that they allow us to consider the synthesized image as the sum of a series of contributions from different parts of the frequency passband. In the derivation of the radio image we assign to  $V$  values  $u_0$  and  $v_0$  which are the true values multiplied by  $\nu_0/\nu$  (Eq. 2-33). The effect in the image can be obtained from the similarity theorem of Fourier transforms (e.g., Bracewell 1978), using which one can write

$$V\left(\frac{\nu_0}{\nu}u, \frac{\nu_0}{\nu}v\right) \rightleftharpoons \left(\frac{\nu}{\nu_0}\right)^2 I\left(\frac{\nu}{\nu_0}l, \frac{\nu}{\nu_0}m\right). \quad (2-35)$$

The coordinates of the brightness function are multiplied by the reciprocal of the factor by which the visibility coordinates are multiplied, and a factor  $(\nu/\nu_0)^2$  appears in the amplitude to conserve the total integrated brightness. One can envision the effect in the synthesis procedure, in which the data over the full receiving bandwidth  $\Delta\nu$  are combined together, as the averaging of a series of images of the same sky brightness distribution, each with a slightly different scale factor and aligned at the  $(l, m)$  origin. The range of variation of the scale factor is equal to the variation of  $\nu/\nu_0$  over the receiving bandwidth. The result of such averaging is clearly to introduce a radial smearing into the brightness distribution, as shown in Figure 2-17b. The angular extent of the smearing at a radial distance  $\sqrt{l^2 + m^2}$  from the origin is approximately equal to  $\frac{\Delta\nu}{\nu_0} \sqrt{l^2 + m^2}$ , and the effect becomes important at distances for which the smearing is comparable with the synthesized beamwidth. An alternative method of imaging with a wide bandwidth is by using a multi-channel receiving system, in which the passband is divided into  $n$  frequency channels of width  $\Delta\nu/n$ . Separate correlators are used for each frequency channel, so the visibility values for each one can be associated with the values of  $u$  and  $v$  corresponding to the center frequency of the channel. Such systems are also used for spectral line observations. In the  $(u, v)$  plane, the elliptical track that represents the projected spacing for any pair of antennas is replaced by a series of  $n$  parallel tracks. In effect, the overall transfer function is the sum of  $n$  single-channel functions, each scaled in  $u$  and  $v$  in proportion to the corresponding center frequency of the receiving channel. The sum of the corresponding images shows no radial smearing (we assume that the smearing corresponding to the channel bandwidth  $\Delta\nu/n$  is negligible), but since the angular scale of the synthesized beam (point spread function) varies from one channel to the next, the effect of averaging the beam profiles is to reduce unwanted sidelobes. Thus the use of a multi-channel system is a desirable technique in broadband image synthesis, but it requires a significant increase in computing to accommodate  $n$  times as many visibility data as in the corresponding continuum observation (see Lecture 21).

## 12. The Effect of Visibility Averaging

The time averaging of the visibility data at the correlator results in another form of smearing of the image. The data from each correlator are separated into consecutive time intervals of length  $\tau_a$ , as shown in Figure 2-18a, and only the average value for each interval is retained. In the subsequent processing the averaged visibility samples are assigned  $(u, v)$  values corresponding to the mid-points of the averaging intervals, although the observed data extend over a range  $\pm\tau_a/2$  relative to each such instant. The effect in the synthesized image can be most easily explained for an observation of a source at the celestial pole. The  $(u, v)$  plane is then normal to the Earth's axis, and the transfer function consists of a series of circles, concentric about the  $u$ - $v$  origin, as in Figure 2-18b. Each circle is generated by a spacing vector rotating with angular velocity  $\omega_e$  equal to that of the Earth. Thus a time offset  $\tau$  in the assignment of  $(u, v)$  values results in a rotation of the visibility function about the  $(u, v)$  origin through an angle  $\omega_e\tau$ . In the Fourier transformation, such a rotation results in an equal rotation of the image. Thus the effect of the time averaging can be envisioned



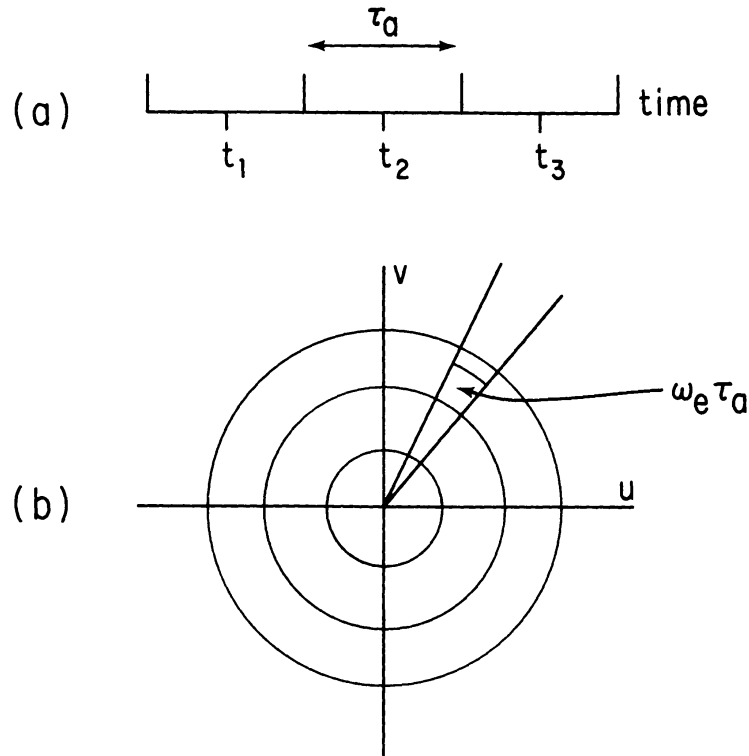


**Figure 2-18.** (a) Consecutive time intervals of duration  $\tau_a$  over which the visibility is averaged. (b) Circular loci in the  $(u, v)$  plane which result from the continuous observation of a source close to the celestial pole. In a time interval  $\tau_a$ , the baselene vectors which generate the loci move through an angle  $\omega_e \tau_a$ .

as an averaging of a series of images that are aligned at the  $(l, m)$  origin, but have angular offsets distributed over a range  $\pm \omega_e \tau_a / 2$ . At a point  $(l, m)$  the extent of the smearing is approximately  $\omega_e \tau_a \sqrt{l^2 + m^2}$ . The direction of the smearing is orthogonal to that resulting from the bandwidth effect, and the two effects are of equal magnitude if  $\Delta\nu/\nu_0 = \omega_e \tau_a$ .

For a source at a lower declination the curves in the transfer function become ellipses, and are centered at the  $(u, v)$  origin only for East–West baselines. In this latter case the expansion of the  $v$ -axis by a factor  $\csc \delta$  restores the circularity, so in an image plane in which the  $m$ -axis (North–South) is compressed by a factor  $\sin \delta$ , the effect is again one of circumferential smearing. In the general case of a non-polar source and non- East–West baselines, the effect of time averaging cannot be described simply in terms of a rotational smearing.

## References

- Arsac, J. 1955, *C. R. Acad. Sci.*, 240, 942–945.  
 Bracewell, R. N. 1966, Report on the Fifteenth General Assembly of URSI, Pub. 1468, National Academy of Sciences (Washington, D.C.), pp. 243–244.

- Bracewell, R. N. 1978, *The Fourier Transform and its Applications*, Second Edition, McGraw-Hill, New York.
- Bracewell, R. N., Colvin, R. S., D'Addario, L. R., Grebenkemper, C. J., Price, K. M., & Thompson, A. R. 1973, *Proc. IEEE*, 9, 1249–1257.
- Christiansen, W. N. & Högbom, J. A. 1985, *Radiotelescopes*, Second Edition, Cambridge University Press (Cambridge, England).
- Fomalont, E. B. 1973, *Proc. IEEE*, 61, 1211–1218.
- Fomalont, E. B. & Wright, M. C. H. 1974, in *Galactic and Extragalactic Radio Astronomy*, First Edition, G. L. Verschuur & K. I. Kellermann, Eds., Springer-Verlag, New York, pp. 256–290.
- Frater, R. H. 1984, *Proc. Astron. Soc. Australia*, 5, 440–445.
- Granlund, J., Thompson, A. R., & Clark, B. G. 1978, *IEEE Trans. Electromag. Compat.*, EMC-20, 451–453.
- Högbom, J. A. & Brouw, W. N. 1974, *A&A*, 33, 289–301.
- Meeks, M. L., Ed. 1976, *Methods of Experimental Physics*, Vol. 12C, Academic Press, New York; see chapters on interferometry.
- Michelson, A. A. 1890, *Phil. Mag.*, Ser. 5, 30, 1–21.
- Moffet, A. T. 1968, *IEEE Trans. Antennas Propagat.*, AP-16, 172–175.
- Napier, P. J., Thompson, A. R., & Ekers, R. D. 1983, *Proc. IEEE*, 71, 1295–1320.
- Napier, P. J., Bagri, D. S., Clark, B. G., Rogers, A. E. E., Romney, J. D., Thompson, A. R., & Walker, R. C. 1994, *Proc. IEEE*, 82, 658–672.
- Preston, R. A., Burke, B. F., Doxsey, R., Jordan, J. F., Morgan, S. H., Roberts, D. H., & Shapiro, I. I. 1983, in *Very Long Baseline Interferometry Techniques*, F. Biraud, Ed., Cepadues (Toulouse, France), pp. 417–431.
- Rohlfs, K. 1986, *Tools of Radio Astronomy*, Springer-Verlag, Berlin.
- Ryle, M. 1952, *Proc. Roy. Soc.*, 211A, 351–375.
- Ryle, M. 1962, *Nature*, 194, 517–518.
- Ryle, M. 1972, *Nature*, 239, 435–438.
- Swenson, G. W., Jr. & Mathur, N. C. 1968, *Proc. IEEE*, 56, 2114–2130.
- Thompson, A. R., Clark, B. G., Wade, C. M., & Napier, P. J. 1980, *ApJS*, 44, 151–167.
- Thompson, A. R. & D'Addario, L. R. 1982, *Radio Science*, 17, 357–369.
- Thompson, A. R., Moran, J. M., & Swenson, G. W., Jr. 1986, *Interferometry and Synthesis in Radio Astronomy*, John Wiley & Sons, New York.
- Walker, R. C. 1984, in *Indirect Imaging*, J. A. Roberts, Ed., Cambridge University Press (Cambridge, England), pp. 53–65.